Solution Structure and Dynamics of the Reduced and Oxidized Forms of the N-Terminal Domain of PilB from *Neisseria meningitidis*[†]

Marc Quinternet,[‡] Pascale Tsan,[‡] Fabrice Neiers,[§] Chrystel Beaufils,[‡] Sandrine Boschi-Muller,[§] Marie-Christine Averlant-Petit,[‡] Guy Branlant,*[,§] and Manh-Thong Cung*[,‡]

Laboratoire de Chimie Physique Macromoléculaire, UMR 7568 CNRS-INPL, Nancy Université, 1 rue Grandville, B.P. 20451, 54001 Nancy Cedex, France, and Maturation des ARN et Enzymologie Moléculaire, UMR 7567 CNRS-UHP, Nancy Université, Faculté des Sciences et Techniques, Bld des Aiguillettes, B.P. 239, 54506 Vandoeuvre-lès-Nancy, France

Received May 13, 2008; Revised Manuscript Received June 24, 2008

ABSTRACT: The secreted form of the PilB protein was proposed to be involved in pathogen survival fighting against the defensive host's oxidative burst. PilB protein is composed of three domains. The central and the C-terminal domains display methionine sulfoxide reductase A and B activities, respectively. The N-terminal domain, which possesses a CXXC motif, was recently shown to regenerate *in vitro* the reduced forms of the methionine sulfoxide reductase domains of PilB from their oxidized forms, as does the thioredoxin 1 from *E. coli*, *via* a disulfide bond exchange. The thioredoxin-like N-terminal domain belongs to the cytochrome maturation protein structural family, but it possesses a unique additional segment $_{(99)}$FLHE$_{(102)}$ localized in a loop. This segment covers one edge of the active site in the crystal structure of the reduced form of the N-terminal domain of PilB. We have determined the solution structure and the dynamics of the N-terminal domain from *Neisseria meningitidis*, in its reduced and oxidized forms. The FLHE loop adopts, in both redox states, a well-defined conformation. Subtle conformational and dynamic changes upon oxidation are highlighted around the active site, as well as in the FLHE loop. The functional consequences of the cytochrome maturation protein topology and those of the presence of FLHE loop are discussed in relation to the enzymatic properties of the N-terminal domain.

Various pathogenic and invasive bacteria such as *Neisseria meningitidis* have recourse to methionine sulfoxide reductase (Msr)[1] to repair oxidative damages caused on protein methionine residues by the immune system of their host. Two stereospecific Msrs reduce, back to methionine, one of the two isomers of the methionine sulfoxide function (MetSO) formed upon oxidation. MsrA is specific of the Met-(*S*)-SO, while MsrB reduces only the Met-(*R*)-SO. Although completely distinct in both their primary, secondary, and tertiary structures, MsrA and MsrB follow a similar three-step catalytic mechanism involving in the last step the reduction, by thioredoxin (Trx), of the oxidized Msr under disulfide state (*1*–*3*). Examples of the fusion of the MsrA and MsrB domains into a single protein are known. In that context, the PilB proteins from *Neisseria* genus, *Fusobacterium nucleatum*, and *Psychrobacter cryohalolentis*[2] are unique in that they possess a supplementary N-terminal domain. In fact, two protein forms in *Neisseria gonorrheae* were shown to be produced *in vivo* (*4*). One form, which contains the three domains, i.e., the N-terminal domain and the central and C-terminal domains that display MsrA and MsrB activities, respectively (*2*), is secreted from the bacterial cytoplasm to the outer membrane, whereas the second form, which is cytoplasmic, only contains the Msr domains. The secreted form was proposed to be involved in the pathogen survival fighting against the defensive host's oxidative burst.

Recently, the N-terminal domain (NterPilB) from *Neisseria meningitidis* was shown to display disulfide oxidoreductase activity toward the PilB Msr domains *in vitro* (*5*). The structure in its reduced form (NterPilB$_{red}$) as well as that from *N. gonorrheae* was determined by X-ray crystallography (*6, 7*). The analysis of NterPilB$_{red}$ X-ray structure from *N. meningitidis* (*6*) has revealed strong structural

[†] This research was supported by the CNRS, the Universities of Nancy I and INPL, the IFR 111 Bioingénierie, the Association pour la Recherche sur le Cancer (ARC-N° 5436), and the French Ministry of Research (ACI BCMS047). F.N. and M.Q. gratefully thank the French Ministry of Research, the CNRS, and the Région Lorraine for financial support.

* To whom correspondence should be addressed. M.-T.C.: phone, (33) 3 83 17 51 07; fax, (33) 3 83 37 99 77; e-mail, Manh-Thong.Cung@ensic.inpl-nancy.fr. G.B.: phone, (33) 3 83 68 43 04; fax, (33) 3 83 68 43 07; e-mail, guy.branlant@maem.uhp-nancy.fr.

[‡] Laboratoire de Chimie Physique Macromoléculaire, UMR 7568 CNRS-INPL, Nancy Université.

[§] Maturation des ARN et Enzymologie Moléculaire, UMR 7567 CNRS-UHP, Nancy Université.

[1] Abbreviations: CMP, cytochrome maturation protein; CSA, chemical shift anisotropy; DTT, dithiothreitol; HSQC, heteronuclear single-quantum coherence; Met-(*S*)-SO, L-methionine (*S*)-sulfoxide; Met-(*R*)-SO, L-methionine (*R*)-sulfoxide; Msr, methionine sulfoxide reductase; NMR, nuclear magnetic resonance; NOE, nuclear Overhauser effect; NOESY, NOE spectroscopy; NterPilB, N-terminal domain of PilB protein from *Neisseria meningitidis*; rms, root mean square; rmsd, rms deviation.

[2] The PilB organization from the *Neisseria* genus is also present in the genome of *Fusobacterium nucleatum*, a Gram-negative anaerobe human opportunistic pathogen, and of *Psychrobacter cryohalolentis*, a Gram-negative coccobacille capable of growth at temperatures below 4 °C.

10.1021/bi800884w CCC: $40.75
Published on Web 07/24/2008

homologies with DsbEs.[3] DsbEs like CcmG from *Escherichia coli* (*8*), CycY from *Bradyrhizobium japonicum* (*9*), TlpA from *Bradyrhizobium japonicum* (*10*), and ResA from *Bacillus subtilis* (*11*) are enzymes which are involved in cytochrome maturation pathway. Like the X-ray structures of these cytochrome maturation proteins (CMPs) (*12–15*), the overall structure of NterPilB consists of a Trx-like fold defined as a mixed four-stranded β-sheet surrounded by three α-helices, with two insertions compared to the canonical Trx-fold. The first insertion, from Val33 to Lys56 residues, is located in the N-terminal region, the numbering following that of the entire PilB from *N. meningitidis* (*2*). The second insertion, from Phe99 to Asn126 residues, gives rise to an additional β-strand and an α-helix. However, NterPilB differs from the CMPs by the presence of an additional loop $_{(99)}$FLHE$_{(102)}$ in the second insertion, near the active site. Recently, Zhang et al. (*16*) have solved by NMR the solution structures of the reduced and oxidized forms of YkuV from *B. subtilis* whose function remains to be determined but which possesses a CMP topology, with an additional loop as NterPilB.

In the present study, we have determined the solution structure of NterPilB in its reduced (NterPilB$_{red}$) and oxidized (NterPilB$_{ox}$) forms and characterized their dynamic properties. The results are compared between the two redox forms so as to detect possible structural or dynamic changes occurring upon the formation of the disulfide bond between Cys67 and Cys70. The functional consequences of the CMP topology and those of the presence of FLHE loop are discussed in relation to the enzymatic properties of NterPilB.

MATERIALS AND METHODS

Sample Preparation. The *E. coli* strain used for NterPilB (Δ33−175) production was BL21-DE3 pLysS transformed with a pETNterPilB plasmid. ^{15}N- and ^{15}N/^{13}C-labeled samples were prepared by growing cells in a minimal media with $^{15}NH_4Cl$ as the sole nitrogen source and with glucose, ^{13}C-labeled or not, as the only carbon source. The Nter-PilB production was induced at an OD_{600} of 0.6 by addition of 1 mM IPTG and harvested after 4 h for the ^{15}N/^{13}C protein and 16 h for the ^{15}N protein. Purification was done as previously described (*5*), and sample purity and molecular mass were checked by SDS−PAGE and electrospray mass spectrometry, respectively. The oxidation of the NterPilB was achieved by incubating NterPilB (0.5 mM) with 5,5′-dithiobis(2-nitrobenzoic acid) (DTNB) (1 mM) in a degassed solution of 10 mM phosphate buffer, pH 7.0 at room temperature, for 10 min whereas the reduced form sample was kept in its reduced state by adding 50 mM 1,5-dithiothreitol-d_{10}. The two samples were isolated by gel filtration on an Econo-Pac 10 DG column (Bio-Rad Laboratory) equilibrated with 10 mM phosphate buffer, pH 7.0. The oxidation state of the N-terminal domain was checked by titration with DTNB as previously described (*5*). The NMR sample contained 0.5 mM protein concentration (95% H_2O, 5% D_2O) in 30 mM phosphate buffer at pH 7.0 (Cambridge Isotope Laboratories).

NMR Spectroscopy. All spectra were acquired at 298 K on a Bruker DRX 600 MHz spectrometer equipped with a TCI cryoprobe. Spectra were processed using the program XWINNMR (Bruker) and analyzed with the programs XEASY (*17*) and CARA (*18*). TSP-d_4 (Euriso-top) was used as an internal reference for ^{1}H chemical shift whereas indirect referencing was used for ^{13}C and ^{15}N chemical shifts (*19*). Backbone amide ^{1}HN, ^{15}N, $^{13}C^{\alpha}$, $^1H^{\alpha}$, $^{13}C'$, and side-chain ^{1}H, ^{13}C resonances were assigned using ^{1}H−^{15}N HSQC, HNCO, HN(CA)CO, HNCA, HN(CO)CA, CBCANH, CBCA(CO)NH, and HNHA experiments. HNHB, HCCH-TOCSY, CC(CO)NH, and ^{1}H−^{15}N, ^{1}H−^{13}C HSQC-NOESY spectra at two different mixing times (70 and 100 ms) were also performed for side-chain assignments. Hydrogen bonds were identified using slow amide proton exchange in D_2O solution (*20*) and temperature dependence at five different temperatures (287, 291, 296, 298, and 305 K) (*21*).

Structure Calculations. Interproton distance restraints were derived from three-dimensional ^{1}H−^{13}C/^{15}N HSQC-NOESY experiments. The NOE cross-peaks were first classified as strong, medium, and weak and converted into upper limits of 2.5, 3.5, and 5.5 Å and then refined after the first run of calculation. Restraints for the pseudoatoms were systematically overestimated. Each hydrogen bond restraint was defined as a couple of distance restraints with an upper limit of 2.4 Å between the acceptor heavy atom and the hydrogen atom and an upper limit of 3.3 Å between the acceptor and donor heavy atoms. Restraint for the disulfide bond was defined as a set of three distance restraints: the distance between the two sulfur atoms S^{γ}_i and S^{γ}_j lies between 2.0 and 2.1 Å; the distance between the C^{β}_i and S^{γ}_j lies between 3.0 and 3.1 Å; the distance between S^{γ}_i and C^{β}_l lies between 3.0 and 3.1 Å. Torsion restraints for the Φ and Ψ angles were derived from the program TALOS (*22*), and all of the peptide bonds were kept planar and *trans*, with the exception of that between Tyr139 and Pro140 which was restrained to be planar and *cis*, on the basis of the C^{β} and C^{γ} chemical shifts of Pro140 ($\delta_C{}^{\beta} = 35.44$ ppm, $\delta_C{}^{\gamma} = 25.21$ ppm) (*23*).

A total of 1000 randomized structures were calculated, and the simulated annealing process was performed for the reduced and the oxidized forms of NterPilB using respectively the programs DYANA (*24*) and CYANA (*25*). The 20 structures with the lowest target function were selected and refined using DISCOVER (Accelrys Inc., San Diego, CA). Figures were drawn with the programs MOLMOL (*26*) and INSIGHT II.

^{15}N Relaxation Experiments. The ^{15}N longitudinal relaxation rate (R_1), ^{15}N transverse relaxation rate (R_2), and the steady-state {^{1}H}−^{15}N heteronuclear NOE experiments were recorded at 298 K on a Bruker 600 MHz spectrometer, using the usual pulse sequences (*27*). A total of 256 (^{15}N) and 2048 (^{1}H) complex points were collected for the R_1 and R_2 experiments, with 8 transients/increment and a recycle delay of 5 s. Ten inversion recovery delays of 2, 50, 100, 200, 300, 400, 600, 800, 1000, and 1200 ms were used for R_1 measurement, whereas eight delays of 8, 16, 32, 48, 64, 80, 112, and 144 ms were used during the CPMG (Carr−Purcell−Meiboom−Gill) period of the R_2 experiments. {^{1}H}−^{15}N

[3] Abbreviations: DsbE, disulfide bond formation; CcmG, cytochrome *c* maturation protein from *Escherichia coli*; TlpA, membrane-anchored thioredoxin-like protein from *Bradyrhizobium japonicum*; CycY, membrane-anchored periplasmic thioredoxin-like protein from *Bradyrhizobium japonicum* (it is the product of *cycY*, the last gene in a cluster of cytochrome *c* biogenesis genes); ResA, extracytoplasmic membrane-bound thiol−disulfide oxidoreductase required for cytochrome *c* maturation in *Bacillus subtilis*; YkuV, protein encoded by the *ykuV* gene from *Bacillus subtilis*.

NOE spectra were recorded in an interleaved way with and without proton saturation during relaxation delay, using 256 × 2 (^{15}N) and 2048 (^{1}H) complex points and 56 transients/increment typically. The ^{15}N saturation was achieved by the application of 120° ^{15}N pulses separated by 5 ms, for a period of 4 s. Spectral widths for all heteronuclear experiments were 2433 Hz (^{15}N) and 8389 Hz (^{1}H) with carrier frequencies at 117.6 and 4.70 ppm, respectively. Data were processed using XWINNMR (Bruker). They were zero-filled in the ^{15}N dimension and apodized with shifted square sine-bell window in both dimensions.

Backbone Dynamics Analysis. NMRVIEW software (*28*) version 6.6.2 was used to measure the peak heights of the ^{15}N−^{1}H cross-peaks and to determine the R_1 and R_2 values from a fit to a single-exponential decay function and also the {^{1}H}−^{15}N heteronuclear NOE from the ratio between the intensities of a peak in the spectra collected with and without proton saturation, respectively. All experiments were performed twice to provide an estimation of the uncertainty on R_1, R_2, and NOE values.

R_1, R_2, and NOE relaxation parameters were analyzed by means of reduced spectral density mapping at $J_{eff}(0)$, $J(\omega_N)$, and $\langle J(\omega_H)\rangle$ values (*29–32*), using a chemical shift anisotropy of −160 ppm for the backbone amide group (*33*) and a NH bond length of 1.02 Å. $J_{eff}(0)$ denotes that the exchange contribution to R_2 is not explicitly considered (*34*). $\langle J(\omega_H)\rangle$ is the average of $J(\omega_H)$, $J(\omega_H + \omega_N)$, and $J(\omega_H - \omega_N)$ which can be approximated by $J(0.87\omega_H)$ (*29*).

Tensor2 (*35*) was used for the Lipari−Szabo analysis (*36, 37*) of the backbone ^{15}N relaxation parameters. Only residues in secondary structure elements were used for determination of the overall tumbling.

pH Titration. A 0.5 mM sample of NterPilB in 10 mM phosphate buffer initially at pH 7 was used for the chemical shift titration. The pH was adjusted by adding small volumes of 1 N HCl or NaOH solutions. TROSY experiments were recorded at nine pH values: 5.50, 6.05, 6.56, 6.88, 7.13, 7.41, 7.71, 8.11, and 8.61 for the reduced form; 5.53, 5.92, 6.29, 6.68, 6.93, 7.30, 7.69, 8.04, and 9.02 for the oxidized form. The pH of the sample was measured before and after the recording of each spectrum, and the average value was taken as the effective pH. Proton chemical shifts of each residue were fitted to $\delta_{obs} = \delta_d + \Delta\delta/[1 + 10^{(pH-pK_a)}]$ using KALEIDAGRAPH (Synergy Software, Reading, PA).

RESULTS

Structure Calculations of NterPilB$_{red}$ and NterPilB$_{ox}$. NterPilB has been studied in a soluble form ranging from Val33 to Leu175. The chemical shift assignments for the reduced and oxidized forms have been reported previously (*38, 39*). For these two forms, a nearly complete assignment of the backbone and of the side chains has been realized except for the sequence Val33 to His35, residues Ser137 and Pro171. Residues Thr36, Tyr51, Lys54, and Ala84 on the one hand and residues Val50 and Lys61 on the other hand remain only partially assigned in the reduced and in the oxidized forms, respectively. There are approximately 30% fewer short-range and long-range NOE correlations for the reduced form, mainly in the Ser49-Asp55, Gln109-Pro118, and Ala166-Leu175 regions for which several residues are stacked with others. The corresponding NOE correlations are unclear, which led us to ignore them in the structure calculations.

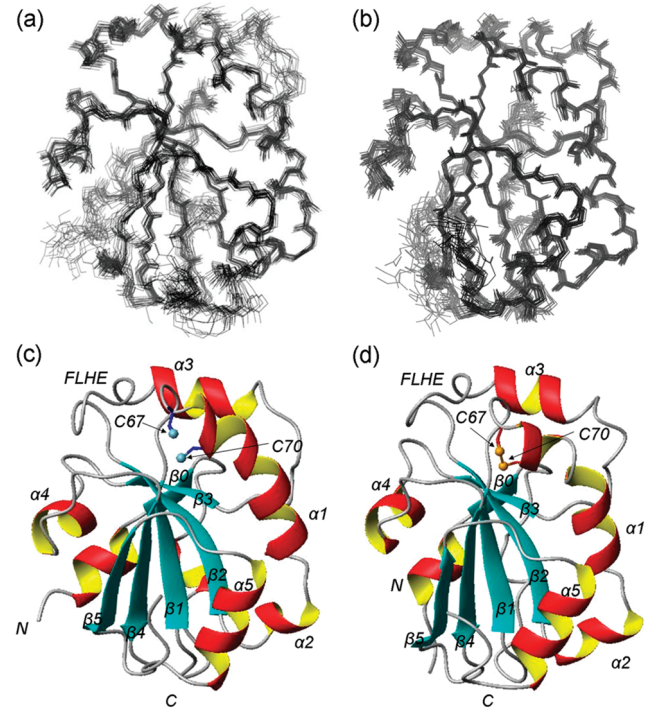

FIGURE 1: Solution structures of both forms, reduced and oxidized, of NterPilB. Backbone superimpositions from Thr39 to Asp170 residues are shown for 20 representative structures of the reduced NterPilB (a) and of the oxidized NterPilB (b). The different secondary structure elements are figured on the most representative structure for the reduced NterPilB$_{red}$ (c) and for the oxidized NterPilB$_{ox}$ (d). The Cys side chains are indicated in blue and red for the reduced and the oxidized forms, respectively. The sulfur atoms of Cys67 and Cys70 are drawn as blue balls for the reduced form and as orange balls for the oxidized form.

The NMR solution structures of both forms were calculated using NOE-derived restraints, backbone dihedral angle restraints derived from TALOS prediction, and hydrogen bond restraints obtained from the ^{1}H/^{2}H exchange combined to the temperature dependence experiments. The superimpositions of the 20 representative structures for each form are shown in Figure 1a,b and the structural statistics for both forms are summarized in Table 1.

For the NterPilB$_{red}$, no distance restraint violation greater than 0.1 Å and no dihedral angle violation greater than 5° are found. According to PROCHECK-NMR analysis, all the non-glycine and the non-proline residues lie in the authorized regions of the Ramachandran plot. For residues Thr39 to Asp170, the 20 structures exhibit an atomic rmsd from the mean structure of 0.79 ± 0.13 Å for the backbone atoms and 1.54 ± 0.13 Å for all heavy atoms. By excluding the regions with high rmsds (Supporting Information Figure S1) and thus keeping only the well-defined Leu40-Ala48, Lys56-Gln109, and Lys119-Leu165 segments which represent 76% of the backbone, the atomic rmsds fall to 0.50 ± 0.08 Å for the backbone atoms and 1.01 ± 0.13 Å for all heavy atoms.

For the NterPilB$_{ox}$, three distance restraint violations greater than 0.1 Å and two dihedral angle violations greater than 5° are observed. According to PROCHECK-NMR analysis, 79.0% of the non-glycine and the non-proline residues remain in the most favored regions of the Ramachandran plot whereas 19.4% of the whole residues are in

Table 1: NMR-Derived Geometrical Restraints and Structural Statistics of the Entire Conformational Set of Reduced NterPilB$_{red}$ and Oxidized NterPilB$_{ox}$

restraint	NterPilB$_{red}$	NterPilB$_{ox}$
upper interproton		
total of distance restraints	2378	2351
intra	819	455
short	485	638
medium	410	428
long	498	671
H-bonds[a]	166	156
SS bond[b]	0	3
dihedral angle	154	169
Φ	77	86
Ψ	77	83
distance violation		
>0.1 Å	0	3
>0.2 Å	0	0
dihedral violation		
>5°	0	2
Ramachandran statistics (PROCHECK-NMR)		
residues in the most favorable region (%)	85.5	79.0
residues in additionally allowed regions (%)	12.6	19.4
residues in generously allowed regions (%)	1.6	0
residues in disallowed regions (%)	0	1.6
rmsd (Å)		
backbone atoms (residues 39−170)	0.79 ± 0.13	0.57 ± 0.13
heavy atoms (residues 39−170)	1.54 ± 0.13	1.27 ± 0.17

[a] Each hydrogen bond is treated as two distance restraints so that 83 hydrogen bonds lead to 166 distance restraints. [b] Each SS bond is treated as three distance restraints.

the additionally allowed regions and 1.6% of the residues (corresponding to Leu100 and to Asp174) are in the disallowed regions. For residues Thr39 to Asp170, the 20 structures exhibit an atomic rmsd from the mean structure of 0.57 ± 0.13 Å for the backbone atoms and 1.27 ± 0.13 Å for all heavy atoms. In the oxidized form, fewer problems of signal overlapping were encountered, which explains that up to 91% of the backbone is well defined (Supporting Information Figure S1). However, if we only retain the previously selected regions (Leu40-Ala48, Lys56-Gln109, and Lys119-Leu165) to provide a comparison with the reduced form, the atomic rmsds become 0.45 ± 0.08 Å for the backbone atoms and 1.07 ± 0.13 Å for all heavy atoms. In these regions, the rmsd values are therefore similar in the two redox states (the comparison between the structures of the two forms leads to rmsds of 0.82 Å for the backbone atoms and 1.22 Å for all heavy atoms).

With the exception of Ala, Gly, and Pro residues, analysis of the χ_1 values and their standard deviations shows that 69% and 64% of residues are well defined respectively for the oxidized and reduced forms. In particular, the low values of standard deviations associated to χ_1 values show that the side chain of most residues of the active site (Trp63-Glu73) and its vicinity (Ser137-Tyr139) and of the loop FLHE (Phe99-Glu102) are well defined. The Φ and Ψ dihedral angles are calculated for the mean structure, and their standard deviations are estimated from those of the 20 representative structures. In parallel to atomic rmsds, all Φ and Ψ dihedral angles are well defined with low standard deviations except for the Met32-Thr36, Asp44-Asn45, Leu52-Lys56, Leu115-Pro118, Asp125-Asn126, Ile136-Ser137, and Ala173-Leu175 sequences for which large standard deviation values are observed and are indicative of less defined structural parts. Conformational changes are highlighted by the large difference of the Φ and Ψ dihedral angle values by comparing

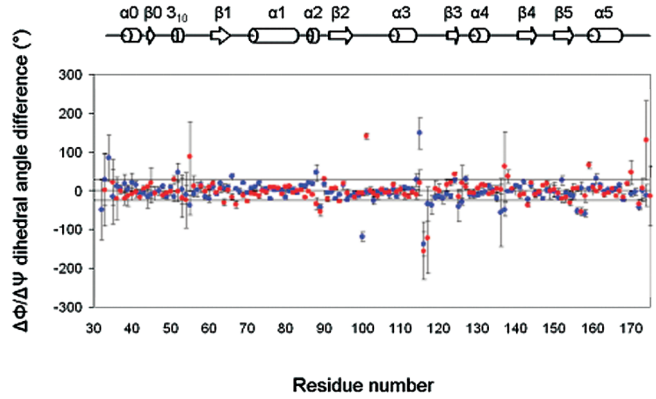

FIGURE 2: Graphical representation of the difference of Φ and Ψ dihedral angle values between the reduced and the oxidized forms along the amino acid sequence of NterPilB. The red and the blue circles represent the variation of Φ and Ψ values upon redox state, respectively. The horizontal lines at 25° and −25° delimit the regions that undergo significant Φ and Ψ dihedral angle changes. Secondary structures, derived from the NMR structures, of the NterPilB are shown above.

the well-defined parts of NterPilB (Figure 2). The standard deviations of the dihedral value differences are taken as the sum of the individual standard deviations of Φ and Ψ calculated for the reduced and oxidized forms.

Structure Analysis of Reduced and Oxidized NterPilB. The overall structures of NterPilB$_{red}$ and NterPilB$_{ox}$ are very similar (Figure 1c,d). The core of both forms exhibits mainly a five-stranded β-sheet composed of parallel (p) and antiparallel (a) individual strands. These latter are arranged in a β3(p)β2(p)β1(a)β4(a)β5(a) pattern and comprise consensually, in both forms, residues Thr58 to Phe62 for β1, Asn90 to Ala95 for β2, Val122 to Thr125 for β3, Ser 141 to Ile145 for β4, and Val151 to Val155 for β5. This main β-sheet network is flanked by five helices comprising consensually residues Pro68 to Trp80 for α1, Ala84 to Ser87 for α2, Asp107 to Tyr112 for α3, Thr129 to Ser133 for α4, and Glu161 to Arg169 for α5. In NterPilB$_{red}$, the five helices are α-type helices. In NterPilB$_{ox}$, the α-helix α1 is split into two helices separated by a turn formed by residues Ser72 and Glu73, and the helix α2 is defined as a 3$_{10}$-helix instead of an α-helix.

The detection of hydrogen-bonded NH groups in the N-terminal region (residues Val33 to Thr39) suggests that this segment may adopt an α-helix organization (helix α0). However, probably due to the lack of NOE-derived and dihedral informations on these residues, no well-defined secondary structure is obtained, in particular for NterPilB$_{ox}$. The large dispersion of this segment, as indicated by its high rmsd values (1.57 ± 0.67 Å and 0.99 ± 0.43 Å for the backbone of NterPilB$_{ox}$ and NterPilB$_{red}$ respectively), probably disturbs the stabilization of the β0 strand. Indeed, an additional little antiparallel β0 strand, comprising the residues Lys41 and Thr42, is present in 14 out of the 20 selected structures of NterPilB$_{red}$ and in 10 out of the 20 selected structures of NterPilB$_{ox}$. Moreover, an additional 3$_{10}$-helix comprising residues Ala48 to Tyr51 is present in 17 of the 20 selected structures of Nter-PilB$_{red}$ and only in 8 of the 20 selected structures of Nter-PilB$_{ox}$, this probably due to the poor assignment of Val50 in the oxidized form in spite of measured hydrogen-bonded NH groups.

Two other regions, far from the active site and for which few NOEs are observed, are also ill-defined: in the vicinity

of Lys54 in both redox forms, and the 113−117 segment, especially in the reduced form. For these segments and for the N- and C-terminal parts, the Φ and Ψ dihedral angle values differ notably between the reduced and oxidized forms. The standard deviation, calculated for the dihedral value differences in these regions which exhibit few NMR restraints, is high (Figure 2). Thus, these differences are not significant. On the other hand, large and significant $\Delta\Phi$ ($\Phi_{ox} - \Phi_{red}$) and $\Delta\Psi$ ($\Psi_{ox} - \Psi_{red}$) differences of the backbone dihedral angle values [$\Delta\Phi$ for Ala64 (−30.1 ± 8.4 °), Cys67 (−36 ± 9.6 °), Cys70 (−27.4 ± 4.2 °), His101 (141.1 ± 7.6 °), Val138 (37.8 ± 17.2 °), Gly157 (−54.5 ± 9.7 °), Ile159 (66.4 ± 9 °) and $\Delta\Psi$ for Trp66 (36.8 ± 7.4 °), Leu100 (−119.2 ± 11.8 °), Ser 137 (−49.3 ± 17.5 °), Lys156 (−52.4 ± 8.1 °), Ser158 (−58.5 ± 9.8 °), Glu161 (32.9 ± 12 °), superior to 25° and combined with a weak standard deviation] upon redox change of Nter-PilB are observed for Cys67, Cys70, and neighboring residues (Ala64 and Trp66), as well as for particular residues located in the β2-α3 and β5-α5 loops, that denotes a rearranging of some active site segments.

Analysis of the ^{13}C chemical shift differences of backbone carbonyl groups reveals regions of significant variation between the reduced and the oxidized forms of NterPilB (Supporting Information Figure S2). Residues surrounding the active cysteines are principally perturbed. That concerns residues Phe62, Ala64, Ser65, Cys67 to Ser72, Phe99 to His101, Pro140, and Ser141. These chemical shift data are consistent with the previously reported data concerning backbone amide groups (*39*) and with local structural changes in the neighborhood of the active site occurring upon oxidation. Other but isolated residues are also perturbed (Leu37, Ala43, Leu52, and Gly118).

^{15}N Relaxation Parameters. The ^{15}N longitudinal relaxation rate (R_1), ^{15}N transverse relaxation rate (R_2), and the steady-state {^{1}H}−^{15}N heteronuclear NOE values of NterPilB were measured for 121 and 122 backbone NH groups out of the 135 nonproline residues, respectively in the reduced and oxidized forms (Figure 3). The unanalyzed residues were either unassigned or overlapped. The average values for the backbone ^{15}N nuclei are very similar in the two redox states: $\langle R_1\rangle = 1.57 \pm 0.02$ s^{-1}, $\langle R_2\rangle = 10.3 \pm 0.3$ s^{-1}, $\langle$NOE$\rangle = 0.80 \pm 0.02$ s^{-1} in the reduced form and $\langle R_1\rangle = 1.55 \pm 0.04$ s^{-1}, $\langle R_2\rangle = 10.9 \pm 0.2$ s^{-1}, $\langle$NOE$\rangle = 0.82 \pm 0.02$ s^{-1} in the oxidized form. The relaxation parameters plotted versus the polypeptidic sequence globally display similar profiles in the two redox forms. For instance, a sharp drop of all three parameters is found within the C-terminus. But the most striking point is a particularly large R_2 value for residue His101 in the reduced form.

Reduced Spectral Density Mapping. Reduced spectral density mapping, which does not require any model for the global motion and for the internal motion, was used first to analyze the relaxation data. $J_{eff}(0)$, $J(\omega_N)$, and $\langle J(\omega_H)\rangle$ spectral density values were calculated for the 121 and 122 NH groups for which the relaxation parameters could be determined respectively in the reduced and oxidized state (see Materials and Methods). As shown in Figure 4, the variations of spectral density values along the sequence are globally similar in both redox states. For instance, a decrease of $J_{eff}(0)$ together with an increase of $\langle J(\omega_H)\rangle$ is observed within the C-terminus, and to a lesser extent around residues Lys53 and Ser158. This indicates flexibility in the C-terminal tail, as well as in the 3_{10}-β1 and β5-α5 loops. Similar decreases in these regions are observed for the $J(\omega_N)$ values, which are found to exhibit a pattern rather similar to that of $J_{eff}(0)$, exept residues undergoing chemical exchange. Indeed, in both redox states, $J_{eff}(0)$ value of residue His101 is clearly higher than the average one, suggesting a large μs-ms time scale chemical exchange. However, in the oxidized form, this value is not as high as in the reduced form. Chemical exchange is likely to be found too in the segment Cys70-Leu74 and for residue Val138, which display, especially in the oxidized form, $J_{eff}(0)$ values slightly above the average, while their $J(\omega_N)$ and $\langle J(\omega_H)\rangle$ values are not particularly low (*40*).

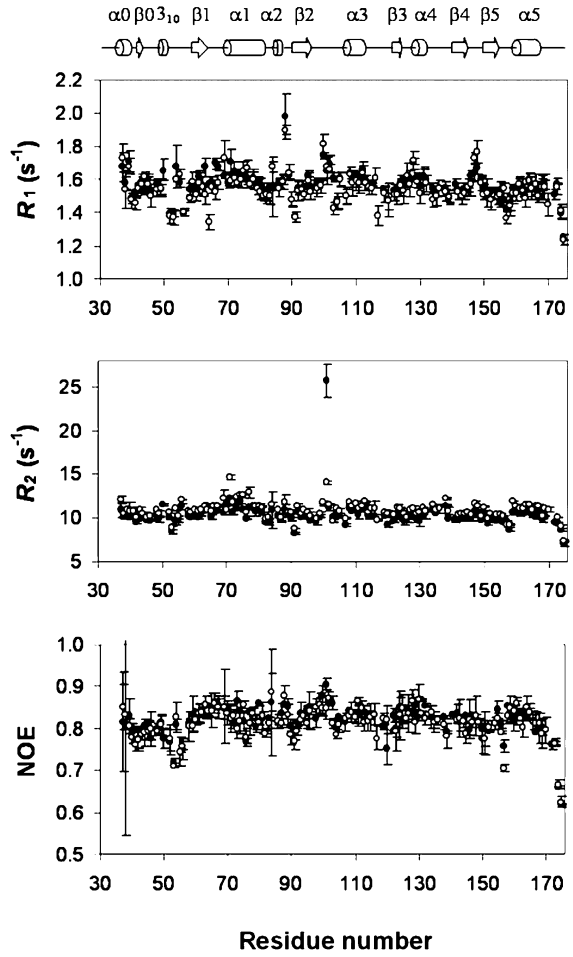

FIGURE 3: ^{15}N longitudinal relaxation rates (R_1), ^{15}N transverse relaxation rates (R_2), and steady-state {^{1}H}−^{15}N heteronuclear NOE values of NterPilB$_{red}$ (filled circles) and NterPilB$_{ox}$ (open circles) versus the amino acid sequence. Experiments were recorded on a Bruker DRX 600 MHz at pH 7.00, 25 °C. The secondary structure is shown at the top.

Differences between the two forms can be clearly highlighted when the differences between spectral density values are plotted. Indeed, two main regions, the segment Trp63-Thr77 containing the Cys-Xaa-Xaa-Cys motif and part of the β2-α3 (FLHE) loop (residues His101-Lys103), appear to exhibit differences larger than two standard deviations from the average (Figure 4) for at least one of the three spectral density values. Remarkably, in the Trp63-Thr77 segment, difference of $J(\omega_N)$ ($\Delta J(\omega_N)$) between the oxidized and reduced forms is mainly negative for residues Trp63-Trp66 in the β1-α1 loop whereas difference of $J_{eff}(0)$

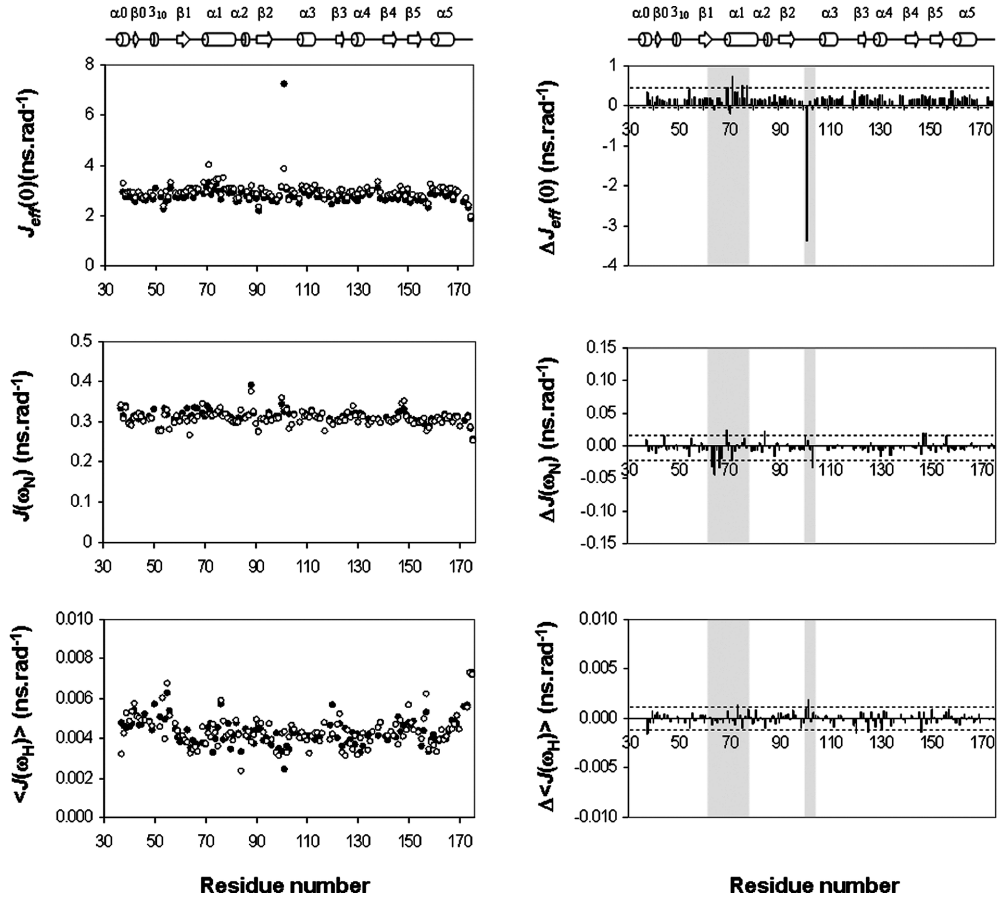

FIGURE 4: Reduced spectral density functions of NterPilB: (a) $J_{eff}(0)$, $J(\omega_N)$, and $\langle J(\omega_H)\rangle$ were obtained for NterPilB$_{red}$ (filled circles) and NterPilB$_{ox}$ (open circles) at 25 °C, pH 7.00, and ^{15}N frequency of 60.81 MHz. (b) Difference of spectral density functions $\Delta J_{eff}(0)$, $\Delta J(\omega_N)$, and $\Delta\langle J(\omega_H)\rangle$ between the oxidized form and the reduced form. The dotted lines represent the limits, defined as the average value ± 2 standard deviations, out of which the difference is considered as significant. The gray boxes highlight the two main regions (63−77 and 101−103) displaying significant changes upon oxidation.

($\Delta J_{eff}(0)$) is mainly positive for residues Leu69-Thr77 at the beginning of the α1 helix. This indicates that the formation of the disulfide bridge leads to a slight decrease of fast time scale motions in the β1-α1 loop containing the catalytic Cys67 together with a slight increase of the slow time scale motions in the α1 helix bearing the recycling Cys70.

Model-Free Analysis. To get a more detailed picture of the dynamics of NterPilB, the relaxation parameters were analyzed with a Lipari−Szabo approach (*36, 37*), by means of the Tensor2 software (*35*) and using the mean NMR structure. An anisotropic tensor giving a global correlation time τ_c of 7.51 ± 0.01 ns and 7.86 ± 0.01 ns, an axial anisotropy of 1.15 and 1.12, and a rhombicity of 1.06 and 1.04 respectively in the reduced and the oxidized forms was found. These values as well as the orientation of the tensor axes are in agreement with the molecule inertia tensor (the principal components of which are in the ratios 1:0.93:0.68), indicating a monomeric state.

Internal mobility parameters were obtained for Lys104 and Phe108 residues respectively in the reduced and in the oxidized forms. A few residues, including the catalytic cysteine Cys67, Leu100, and Lys103 in the reduced form, and the recycling Cys70, residues Gly98-Leu100, Glu102 in the oxidized form, could not be correctly fitted and had therefore to be discarded from the analysis.

The mean order parameter is 0.90 in the reduced form and 0.92 in the oxidized form. In both forms, the order parameter decreases in the 3$_{10}$-β1 loop (residues Leu52 to Lys56), in the β5-α5 loop (residues Lys156 to Ser158), and in the C-terminal region (residues Asn172 to Leu175) as shown in Figure 5. Relatively low values are also found here and there, generally in loops or at the end of some helices or sheets (residues Asp107, Val151). Internal correlation time was found mainly in the regions Lys40-Lys56 and Asp150-Gly157 and in the C-terminus, far from the active site. As expected, a large exchange term R_{ex} is found for residue His101, especially in the reduced state. Smaller R_{ex} terms are also observed in the α1 helix (residues Cys70-Leu74), and the α4-β4 loop (residues Leu134-Val138) and punctually for residues Leu52 and Ile159 in both forms.

pH Titration and pH Effect on Dynamics Parameters. R_{ex} parameter, which indicates chemical exchange, usually reflects conformational exchange. Yet, the residue His101 with surprisingly large R_{ex} value appears to be a His residue, the side chain of which usually has a pK_a around 6.8 in solution, thus very close to the sample pH. Since His101 is located in the critical FLHE loop, a titration study and a relaxation study at different pHs were carried out to determine whether the His101 exchange term originates from large conformational changes or is simply related to the pH conditions.

The ^{1}H and ^{15}N chemical shifts of the backbone and of the tryptophan side-chain NH groups were measured at nine pH values, ranging from pH 9 to pH 5.5. Superimposition

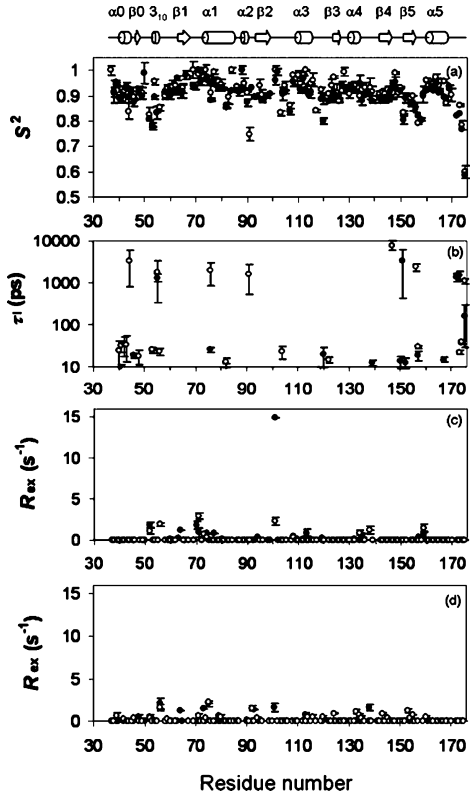

FIGURE 5: Model-free internal mobility parameters of NterPilB: (a) Order parameter S^2, (b) internal correlation time τ_i, and (c) exchange term R_{ex} at pH 7 and (d) exchange term R_{ex} at pH 5.5 for NterPilB$_{red}$ (filled circles) and NterPilB$_{ox}$ (open circles) versus the amino acid sequence. The secondary structure is shown at the top.

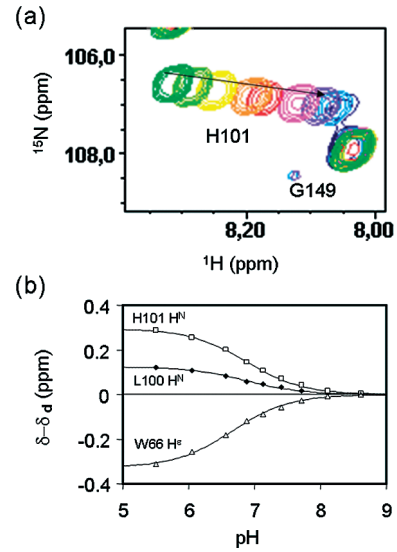

FIGURE 6: pH titration of NterPilB: (a) Overlay of ^{1}H−^{15}N HSQC spectra of NterPilB$_{ox}$ showing His101 and G149 cross-peaks, recorded at pH 5.50 (dark green), 6.05 (light green), 6.56 (yellow), 6.88 (orange), 7.13 (red), 7.41 (pink), 7.71 (purple), 8.11 (light blue), and 8.61 (dark blue). (b) Proton chemical shift titration curves for the backbone NH of Leu100, His101 and the side-chain NH^ε of Trp66. The continuous lines show the best fit to a simple Henderson−Hasselbalch equation.

of the ^{1}H−^{15}N HSQC spectra reveals that most cross-peaks remain unchanged, suggesting that the three-dimensional structure is conserved. The largest variations are observed for the ^{1}H chemical shift of the backbone NH of Leu100, His101 and the side-chain NH^ε of Trp66 in both redox states. These observed chemical shifts correctly fit a simple Henderson−Hasselbalch equation, leading to a pK_a = 6.8 ± 0.1 in both redox states. This pK_a value likely corresponds to that of the His101 imidazole side chain, which is the closest titrable element to those nuclei experiencing large chemical shift variations (Figure 6). Moreover, the solution structure shows that the imidazole ring is exposed to solvent and is therefore expected to have a pK_a value close to that of the free amino acid, which is precisely 6.8.

A new set of relaxation parameters was recorded at pH 5.5 for both redox forms and analyzed with a Lipari−Szabo approach, in the same manner as for pH 7. In both redox states, dynamics results were globally similar to those at pH 7, except that the R_{ex} value of His101 falls dramatically from 14.9 s^{-1} down to 1.9 s^{-1} in the reduced form and equals zero in the oxidized form (Figure 5d).

DISCUSSION

Global Structures and Dynamics of NterPilB in Solution. The solution structure of NterPilB$_{red}$ from *N. meningitidis* exhibits the same folding as the X-ray structure. Backbone superimposition (for residues Thr39 to Asp170) leads to a rmsd of 1.04 Å (Figure 7a). The locations of the secondary structures are similar. The α-helix α_0, the strand β0, and the 3$_{10}$-helix in the N-terminal region, found in the majority of the 20 NMR structures, are present in the X-ray structure. However, exceptions can be highlighted. First, the end of strand β1 is one residue shorter in all NMR reduced structures, as in the X-ray structure of the reduced N-terminal domain of PilB from *N. gonorrheae*. Second, the beginning of helix α1 is slightly bent but continuous, whereas it shows a break at residues Ser72 and Glu73 in the crystal structure. Nevertheless, no drastic changes concerning the side chains of the residues around the active site are observed between the NMR and the X-ray structures of NterPilB$_{red}$ (Figure 7b).

DALI (*41*) and VAST (*42*) have been used to search for structural homologues of the NterPilB$_{red}$ NMR solution structure in the PDB (*43*). In addition to the CMPs previously identified, the newly reported structure of YkuV from *B. subtilis* can be included to the structural comparison with NterPilB and CMPs, based on its scores of superimposition (DALI Z-score = 9.8; VAST-score = 9.8). NterPilB and CMPs all contain a Trx-like fold defined as a mixed four-stranded β-sheet surrounded by three α-helices. A structural alignment of NterPilB, *E. coli* DsbE, and YkuV with *E. coli* Trx1 shows the presence of a long insertion between residues Gln62 and Asn63 of Trx1 (corresponding to residues Gly98 and Gly128 in Figure 8). As described before for NterPilB and CMPs, this segment gives rise to an additional α-helix and a β-strand. Interestingly, this segment in NterPilB and YkuV is longer than in other CMPs and forms an additional loop. These two proteins appear to possess a segment of similar length leading to a YkuV $_{(71)}$RSED$_{(74)}$ loop equivalent in length to the NterPilB $_{(99)}$FLHE$_{(102)}$ loop. NterPilB would therefore be closer to YkuV than other CMPs.

Moreover, our NMR study provides additional dynamics information in solution. The Lipari−Szabo analysis of the relaxation parameters shows that NterPilB is a relatively rigid protein globally, with a mean order parameter of 0.91 for its backbone. Low order parameters in both redox forms are found for the C-terminal extremities, in the 3$_{10}$-β1 loop

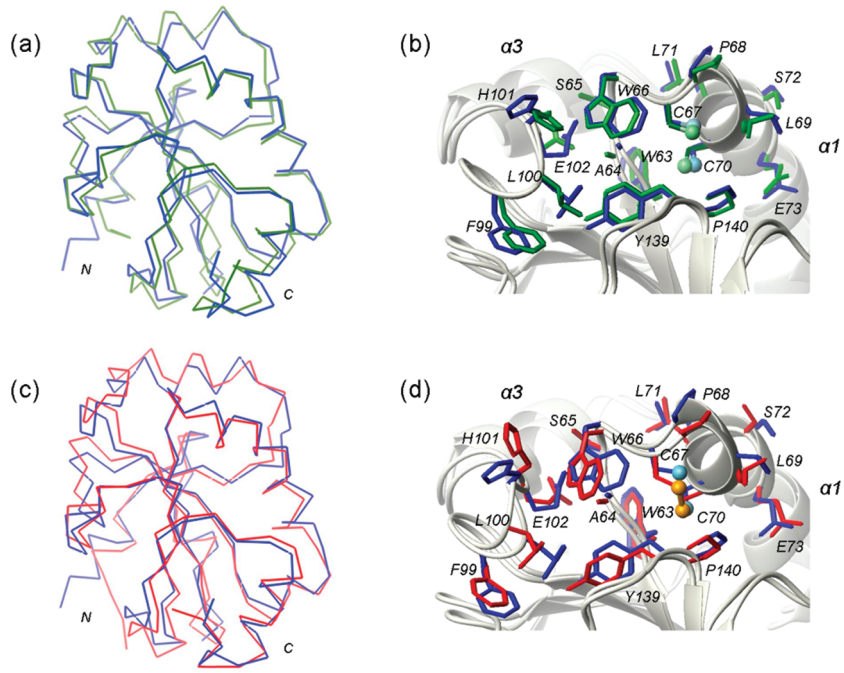

FIGURE 7: Backbone superimposition (from Thr39 to Asp170 residues) of the NMR solution structure (blue) with X-ray structure (green) for the reduced NterPilB (a). Active sites of these two forms are also figured using the same colors (b). Backbone superimposition (from Thr39 to Asp170 residues) of the NMR solution structures of the reduced (blue) and oxidized (red) forms of NterPilB (c). Active sites of these two forms are also figured using the same colors (d). Only heavy atoms of the side chains are represented. The sulfur atoms of Cys67 and Cys70 are drawn as blue balls for the NMR reduced form, as orange balls for the NMR oxidized form, and as green balls for the X-ray reduced form.

(residues Leu52-Lys56) and the β5-α5 loop (residues Lys156-Ser158) as well as for residues Asp107 and Val151 at the beginning of α3 helix and β5 sheet, respectively (Figure 9). The flexibility highlighted in these regions is supported by the reduced spectral density mapping exhibiting low $J_{eff}(0)$ values compensated for by high $\langle J(\omega_H)\rangle$ values. The high rmsd around Lys54, observed both in the solution and in the crystal structures, can therefore be explained by a large backbone flexibility. In contrast, the poor resolution obtained for segment Ala113-Tyr117 in the reduced form is more likely due to a lack of experimental NOEs and angle restraints, as no particular dynamics is observed. Although experimental relaxation data are missing for the first four residues Val33-Thr36, high order parameters are found in the Leu37-Thr39 segment, in agreement with the assumption that the N-terminal region may form an α-helix, as in the crystal structure. Nevertheless, this N-terminal helix would not be well characterized because of the lack of NMR restraints.

In fact, apart for the putative CMP YkuV (*16*), no ^{15}N relaxation studies have been reported yet for CMPs as they were all studied in the crystal state. As far as we know, the only other dynamics data available on homologous proteins are for *Chlamydomonas reinhardtii* oxidized Trx *m* (*44*) and for *E. coli* oxidized and reduced Trxs (*45*). Our dynamics results were therefore discussed in comparison with YkuV and those thioredoxins. The increased flexibility observed for the 3_{10}-β1 loop in NterPilB was also found in the homologous loop of Trxs and YkuV. However, it is located on the opposite side of the active site and may not be of functional importance. In contrast, the flexible β5-α5 loop is part of the active site and the homologous β5-α5 loop, in *C. reinhardtii* (*44*) and *E. coli* (*45*) Trxs, was reported to exhibit low order parameter as well. Unfortunately, this could not be generalized to YkuV since data are missing in this region. However, this loop flexibility, which seems to be recurrent, could be mandatory for its interaction with a biological partner. Interestingly, in the single docking calculated model of YkuV complexed with ArsC, this loop seems to largely participate to interaction. As far as the α4-β4 loop is concerned, slow microsecond to millisecond time scale conformational exchange is found in NterPilB whereas subnanosecond time scale flexibility was reported in the *C. reinhardtii* and *E. coli* Trxs. Conformational exchange is observed in the β1-α1 loop and α1 helix bearing the catalytic and recycling cysteins in NterPilB as well as in *E. coli* Trx reduced form and in YkuV. Whereas a large segment comprising the α2-β3 loop and the β3 strand in YkuV displays significant chemical exchange, only a few residues in the corresponding region of NterPilB have a small R_{ex} contribution. The dynamics differences evidenced in the Trxs and Trx-like proteins, along with the presence of the specific insertion in NterPilB, may contribute to explain the specificities of each protein.

Induced Redox Changes in the Active Site. Backbone superimposition (from Thr39 to Asp170 residues) of NterPilB$_{red}$ and NterPilB$_{ox}$ solution structures leads to a relatively low rmsd value of 1.16 Å, suggesting that the formation of the disulfide bond does not affect dramatically the global folding of the enzyme (Figure 7c). However, the mean distance between the two sulfur atoms of Cys67 and Cys70 decreases from 3.54 ± 0.55 Å to 2.10 ± 0.03 Å in NterPilB$_{red}$ and NterPilB$_{ox}$, respectively. In NterPilB$_{ox}$, the presence of the disulfide bridge seems to freeze the conformation of the beginning of α1 helix and to induce a break (Figure 7c,d). This helix is locally bent by a turn formed with the residues Ser72 and Glu73. The central axis of the two resulting parts of α1 helix shows a larger deviation than in NterPilB$_{red}$.

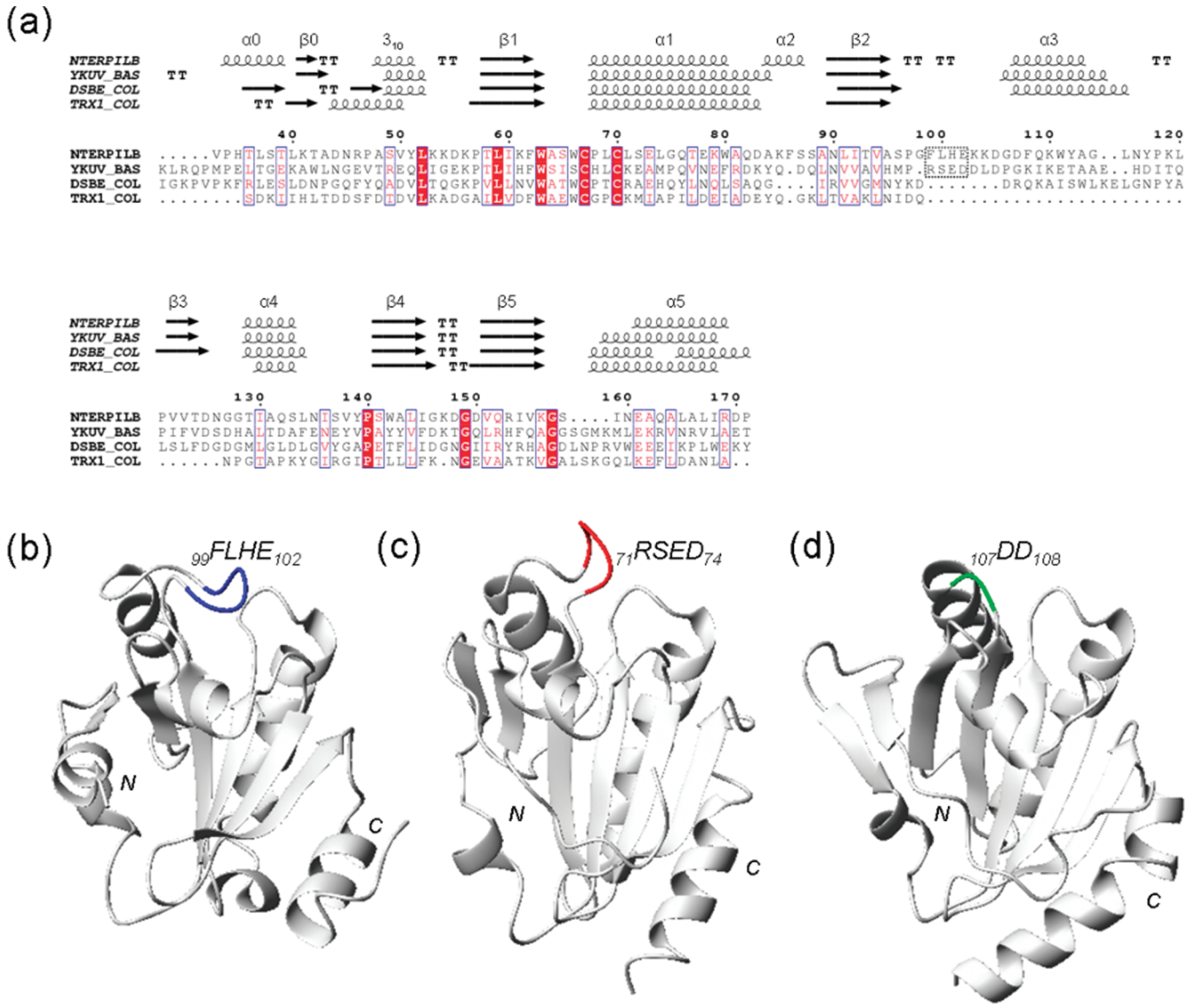

FIGURE 8: Amino acid sequences of NterPilB from *N. meningitidis*, YkuV from *B. subtilis*, and DsbE and Trx1 from *E. coli* were aligned according to their three-dimensional superimposition. Residues on red background are consensually found in all sequences. Residues in blue boxes show nonstrict similarities. Secondary structures were displayed up to the sequence alignment. Annotations were only displayed for NterPilB. The figure was prepared using ESPript (*49*) (a). Backbone symbolic representation of the NMR solution structure of $NterPilB_{red}$ from *N. meningitidis* (b), the NMR solution structure of $YkuV_{red}$ from *B. subtilis* (c), and X-ray structure of $DsbE_{ox}$ from *E. coli* (d). Residues $_{99}$FLHE$_{102}$ in NterPilB are represented in blue; residues $_{71}$RSED$_{74}$ in YkuV (corresponding to residues 98 and 128 in the alignment), in red; and the insertion site $_{107}$DD$_{108}$ in DsbE, in green.

Whatever the oxidation state, the conformation of the active site of both forms appears similar and side chains for residues surrounding the two cysteines lie in the same orientation as shown in Figure 7d. Indeed, except chemical shift variation data suspecting that ResA may undergo localized conformational change between oxidation states (*46*), in the other CMPs crystal structures and YkuV NMR structures, the presence of the disulfide bond seems to not affect dramatically the global Trx-like fold either. One can notice that the break after the first four residues of α1 helix in *N. meningitidis* $NterPilB_{ox}$ NMR solution structures was observed too in the X-ray structures of $NterPilB_{red}$ from *N. meningitidis* and *N. gonorrheae*. On the contrary, in $NterPilB_{red}$ NMR solution structure and in Trx, DsbE, ResA, TlpA, and YkuV structures (in the reduced or oxidized states), this helix can still be considered as continuous, although slightly distorted. The dynamic and structural studies suggest that the 3D structures of both reduced and oxidized forms are well defined, rigid, and almost similar. However, a more in-depth examination of the backbone dihedral angle parameters made it possible to highlight, through the comparison between the Φ and Ψ angle values of the two reduced and oxidized forms, significant structural changes upon oxidation of NterPilB especially concerning the active cysteines and surrounding residues Ala64 and Trp66 and also in the neighboring β2-α3 and β5-α5 loops. This suggests that a fine rearranging of the Trp66-Cys67, Leu69-Cys70, Lys156-Gly157, Ser158-Ile159 bonds and of the Ile136-Val138 segment is concomitant to disulfide bridge formation. The low values of the standard deviations estimated for these differences show that it corresponds to rigid and well-defined structures of protein rather than to ill-defined regions as those where high values of the standard deviations were estimated. These conformational changes are supported by the observation of significant chemical shift

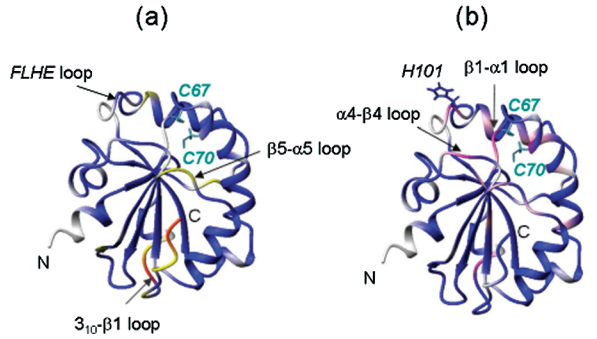

FIGURE 9: Model-free internal mobility parameters of NterPilB$_{red}$: (a) Order parameter S^2. Residues with an order parameter lower than 1 or 2 standard deviations are represented respectively in yellow and dark orange. (b) Residues with an exchange term $0 < R_{ex} < 1$ s^{-1} are represented in light pink and those with $R_{ex} > 1$ s^{-1} in dark pink. Residues for which mobility parameters could not be determined are in white.

variations of backbone carbonyl and amide groups between the two redox states.

As for the dynamic properties, the analysis of Lipari−Szabo mobility parameters showed, in both redox states, relatively high order parameter around the active site as well as the presence of conformational exchange for a few residues. However, these results did not allow to analyze thoroughly the redox changes in the active site, as several residues could not be fitted in this region. Moreover, the observed perturbations could not be considered as significant, given the several assumptions made in the Lipari−Szabo analysis and the general offset of 0.02 for the average order parameter observed between the two redox states, which might originate from the uncertainty in the diffusion tensor determination. The spectral density mapping, which uses the relaxation parameters without any dynamic or structural model hypothesis, could be performed on all residues of the active site, except prolines, and appeared to give complementary valuable information and to be a more suitable method to detect dynamic variations. Indeed, in both redox forms, the $\langle J(\omega_H)\rangle$ values are relatively low or close to the average, all around the active site, except for residue Gln76 which has a slightly decreased order parameter of 0.91. This indicates that this whole region, including the residues that were rejected from the model-free analysis, has very restricted flexibility in the fast time scale. Nevertheless, relatively large $J_{eff}(0)$ values were observed for many residues in the segment Leu69-Gly75, especially in the oxidized form, suggesting the presence of slow movements in the μs-ms range affecting a large part of the active site. The differences of spectral density values between the redox states interestingly show that motions in the slow time scale around the active site are slightly increased in the oxidized state compared to the reduced state ($\Delta J_{eff}(0) > 0$), while those in a faster time scale are decreased ($\Delta J(\omega_N) < 0$).

The Structure of the FLHE Loop. In NterPilB$_{red}$ and NterPilB$_{ox}$ NMR solution structures, the FLHE residues are shaped in a well-structured loop internally stabilized by a hydrogen bond between Phe99 and Glu102. Moreover, a hydrogen bond involving backbone NH group of Ser65 and side chain of Glu102 promotes the global positioning of this four-residue segment. The rmsd values between the NMR solution and X-ray structures of NterPilB$_{red}$ are respectively 0.31 and 1.35 Å for the backbone and the heavy atoms of the FLHE loop. This indicates a high conservation level of this structural element, between the crystal and the solution structures. However, the rmsd value between the reduced and the oxidized NMR structures for this same segment is increased up to 0.61 Å for the backbone atoms and decreased down to 0.99 Å for the heavy atoms. Indeed, the Ψ dihedral angle of Leu100 and the Φ dihedral angle of His101 switch from $35.2 \pm 11.8°$ to $-84.0 \pm 0.8°$ and from $62.1 \pm 7.6°$ to $-156.8 \pm 2.7°$ respectively between the reduced and the oxidized state. This promotes a reorientation of Leu100-CO and His101-NH groups. Even if the global backbone orientation and the side-chain positions for residues Phe99 to Glu102 show no drastic changes, subtle structural differences do exist between reduced and oxidized forms at this precise spot.

The relaxation data have been inspected particularly and cautiously for the FLHE loop. The order parameters observed in the FLHE loop were all higher than 0.91, suggesting very restricted vibrational motions. However, one has to keep in mind that several mobility data are missing in the loop, especially for the residues that could not be reliably fitted by the Tensor2 program. For that reason, a redox comparison of the mobility parameters in the FLHE loop was possible on His101 only, the only residue for which the Lipari−Szabo analysis could be performed in both states. His101 order parameter did not show any significant variation. As far as its exchange term is concerned, the dramatically large value (14.9 s^{-1}) obtained in the reduced form at pH 7 appears to fall down to 1.9 s^{-1} at pH 5.5. Comparable effects have been reported by Hass et al. in plastocyanin (*47*), for its two His, one with a pK_a of 7.1 and the other, ligated to a Cu(I) ion, with a pK_a of 5.1. Indeed, the exchange terms observed for the nuclei close to the His side chain are assigned to the protonation/deprotonation equilibrium of the ionizable group and, therefore, follow a pH-dependent function reaching a maximum for pH = pK_a (*47*). A pH titration from pH 5.5 to 9 of NterPilB showed that Leu100, His101 backbone NHs and the Trp66 side-chain NH$^{\epsilon}$ experienced the largest chemical shift variations, which leads to a pK_a value estimated at 6.8 in both redox states. This pK_a value precisely corresponds to that of the His free amino acid and is logically assigned to the His101 imidazole side chain, which is largely exposed to solvent (Figure 9b). Our results therefore point out that the large exchange term observed at pH 7 for the His101 backbone NH group mostly originates from the protonation/deprotonation of the side chain and not from a large conformational change. This phenomenon is also present in the oxidized form, R_{ex} decreasing from 2.5 s^{-1} at pH 7 to zero at pH 5.5. However, the R_{ex} value at pH 7 is smaller than that in the reduced form, although the pK_a values of His101 side chains were found to be identical in both oxidized and reduced forms. A possible explanation could be the slight conformation change occurring in the His101 backbone, observed by a close inspection of the NMR structures (see above and Supporting Information Figure S3). Indeed, in the reduced state, the His101 amide NH bond is relatively exposed to solvent and globally lies on the same side as its imidazole side chain, in all 20 representative structures. In contrast, in the oxidized state, this NH bond seems to reorient, in all structures, by pointing inside of the protein, i.e., opposite to the N$^{\epsilon}$H of the His101 side chain. Therefore, the His101 NH group in the oxidized state might

be less affected by the occurring protonation/deprotonation process at its side chain than in the reduced state. Finally, the relaxation study detects no large conformational exchange in the FLHE loop in both redox forms, since the exchange term observed for His101 was shown to reflect mostly a proton exchange at the histidine side chain.

As for the active site, the spectral density mapping appeared to be useful to complement the dynamics analysis in the FLHE loop, since it could be performed on all residues and could not be biased by any model assumptions. Rather low $\langle J(\omega_H)\rangle$ values indicative of very restricted flexibility are obtained in the whole loop. Particularly high $\Delta J_{eff}(0)$ values are observed only for His101, which is affected by the proton exchange at its side chain, as discussed above. The spectral density mapping therefore confirms that the FLHE loop is globally rigid in both redox states. However, the differences of spectral density values between the oxidized and the reduced forms highlight significant variations of $J(\omega_N)$ and $\langle J(\omega_H)\rangle$ in this loop, indicating dynamic perturbations on the fast time scale. Finally, together with the subtle conformational changes observed between the two redox states, dynamics results demonstrate the presence of small but significant perturbations upon redox change.

Interestingly, the additional Arg71-Asp77 segment of YkuV that corresponds in NterPilB to the Phe99-Asp105 segment holding the additional FLHE loop (Figure 8a) is equally well structured in the reduced and the oxidized forms of YkuV (backbone rmsd values of 0.47 ± 0.20 and 0.44 ± 0.16 Å, respectively). Nonetheless, the conformation of this segment is clearly different in YkuV and in NterPilB. The protrusion formed by this segment points toward the active site in NterPilB (Figure 8b), while it rather stretches along the β-strand axis and points toward the solvent (Figure 8c) in YkuV. From the simple docking-calculated model of YkuV complexed with ArsC from *B. subtilis*, this loop seems to be close to the interaction interface. However, as observed for the FLHE loop of NterPilB, no particular dynamics data have been reported for the RSED loop of YkuV (*16*). This may suggest that a well-structured segment which does not exhibit large internal motions in the unbound state of the protein could possibly be involved during the binding step with a biological partner. The orientation of this segment relative to the active site may be then a sufficient element to generate the substrate specificity.

Functional Consequences of the CMP Topology and of the Presence of the FLHE Loop. NterPilB is a periplasmic disulfide oxidoreductase belonging to the Trx-like family but with a CMP topology. As *E. coli* reduced Trx1, it is able to regenerate the reduced forms of the Msr domains of PilB from their oxidized forms. But, in constrast to *E. coli* Trx1, (i) $NterPilB_{ox}$ is not reduced by the *E. coli* Trx reductase (*5*), and (ii) $NterPilB_{red}$ does not regenerate the *E. coli* reduced forms of MsrA and MsrB from their oxidized forms (data not shown). Compared to CMPs, one edge of the active site is covered by the specific FLHE loop. Our results show that the reduced and the oxidized forms of NterPilB have in common a few flexible regions. Significant differences in the dihedral angle values upon the redox process of NterPilB are observed for Cys67, Cys70, and neighboring residues (Ala64 and Trp66), as well as for particular residues located in the β2-α3 and β5-α5 loops, that denote a rearranging of some segments near the active site. In particular, the large values of $\Delta\Psi$(Leu100) and $\Delta\Phi$(His101) (Supporting Information Figure S1) attest the rearranging of the Leu100-His101 bond and the reorientation of the His101-NH. However, the FLHE loop keeps very restricted fast time scale motions and experiences no large conformational exchange in both states. These results raise the question of the role of the specific FLHE loop. Two hypotheses can be advanced both as a discriminating factor in the recognition of either its periplasmic recycling partner or the oxidized Msr domains within the PilB protein.

The recycling partner of $NterPilB_{ox}$ is probably the N-terminal domain of DsbD (nDsbD). Indeed, the nDsbD from *E. coli* was shown to be able to reduce $NterPilB_{ox}$ from *N. gonorrheae* (*7*). Recently, our group purified the nDsbD domain from *N. meningitidis* and showed that it efficiently reduces *in vitro* $NterPilB_{ox}$ from *N. meningitidis* with a k_2 value of 6×10^5 M^{-1} s^{-1} (Selme et al., unpublished results). The nDsbD domain of *E. coli* presents an immunoglobulin-like fold and is known to efficiently recycle three periplasmic Trx-like proteins (*48*). These proteins are involved either in the periplasmic disulfide isomerization or in the cytochrome *c* maturation systems, all of them lacking the FLHE loop. These data strongly suggest that the FLHE loop is not a discriminating factor for the interaction with the nDsbD. This is confirmed by the fact that the *N. meningitidis* DsbE, which has been recently purified and characterized by our group, is efficiently reduced by the nDsbD domain with a k_2 value in the range of that determined for the NterPilB domain (Gand et al., unpublished results).

An alternative role of this loop would be to promote a selective interaction between the NterPilB domain and the oxidized Msr domains within the PilB protein. This is probably the case. Indeed, the NterPilB domain has been previously shown to reduce efficiently the isolated MsrB domain of PilB (*5*),[4] while recent results from our group have demonstrated that the *N. meningitidis* DsbE is unable to reduce the isolated oxidized MsrB domain of PilB (Selme et al., unpublished results). In that context, the knowledge of the structure of a complex between NterPilB and the MsrB domain of PilB, linked by a mixed disulfide bond, could allow fine analyses of the interactions between both partners and, in particular, of the role of the FLHE loop. An enzymatic characterization of a truncated form of NterPilB deleted from the FLHE loop would be also informative.

ACKNOWLEDGMENT

Access to the Bruker DRX 600 (NMR facilities of the Service Commun de Biophysicochimie des Interactions, Nancy I) was deeply appreciated. We thank Dr. G. Boussard for critical review of the manuscript and Dr. N. Coudevylle and Dr. S. Bouguet-Bonnet for technical assistance.

SUPPORTING INFORMATION AVAILABLE

Figure S1 shows a backbone rmsd (in Å) distribution as a function of the residue number along the $NterPilB_{red}$ (blue) and $NterPilB_{ox}$ (red) sequence. Figure S2 shows chemical

[4] Previous kinetic studies on the soluble domains of PilB have shown that the NterPilB is able to reduce efficiently the MsrB domain but not the MsrA one (*5*). This latter result is probably due to the fact that the activity was tested on an isolated domain but not on the entire PilB protein. Indeed Brot et al. (*7*) have shown, in the full-length protein context, the absence of a preference for the NerPilB from *N. gonorrheae* to reduce one Msr domain over the second one (*7*).

shift perturbations of the ^{13}C CO backbone groups calculated between the reduced and the oxidized form of NterPilB. The dotted line corresponds to the value of the mean perturbation plus two standard deviations. The measures were done at 600 MHz, 298 K, and pH 7.0 for the two forms. Figure S3 shows the structure close-up of NterPilB around His101. The 20 representative structures of the reduced (blue) and the oxidized (red) state are displayed after backbone superimposition (from Thr39 to Asp170 residues). The backbone amide HN and the side-chain $N^{\epsilon}H$ bonds of His101 are represented in thick lines. This material is available free of charge via the Internet at http://pubs.acs.org.

REFERENCES

1. Boschi-Muller, S., Azza, S., Sanglier-Cianferani, S., Talfournier, F., Van Dorsselear, A., and Branlant, G. (2000) A sulfenic acid enzyme intermediate is involved in the catalytic mechanism of peptide methionine sulfoxide reductase from *Escherichia coli*. *J. Biol. Chem. 275*, 35908–35913.
2. Olry, A., Boschi-Muller, S., Marraud, M., Sanglier-Cianferani, S., Van Dorsselear, A., and Branlant, G. (2002) Characterization of the methionine sulfoxide reductase activities of PILB, a probable virulence factor from *Neisseria meningitidis*. *J. Biol. Chem. 277*, 12016–12022.
3. Boschi-Muller, S., Olry, A., Antoine, M., and Branlant, G. (2005) The enzymology and biochemistry of methionine sulfoxide reductases. *Biochim. Biophys. Acta 1703*, 231–238.
4. Skaar, E. P., Tobiason, D. M., Quick, J., Judd, R. C., Weissbach, H., Etienne, F., Brot, N., and Seifert, H. S. (2002) The outer membrane localization of the *Neisseria gonorrhoeae* MsrA/B is involved in survival against reactive oxygen species. *Proc. Natl. Acad. Sci. U.S.A. 99*, 10108–10113.
5. Wu, J., Neiers, F., Boschi-Muller, S., and Branlant, G. (2005) The N-terminal domain of PILB from *Neisseria meningitidis* is a disulfide reductase that can recycle methionine sulfoxide reductases. *J. Biol. Chem. 280*, 12344–12350.
6. Ranaivoson, F. M., Kauffmann, B., Neiers, F., Wu, J., Boschi-Muller, S., Panjikar, S., Aubry, A., Branlant, G., and Favier, F. (2006) The X-ray structure of the N-terminal domain of PILB from *Neisseria meningitidis* reveals a thioredoxin-fold. *J. Mol. Biol. 358*, 443–454.
7. Brot, N., Collet, J. F., Johnson, L. C., Jönsson, T. J., Weissbach, H., and Lowther, W. T. (2006) The thioredoxin domain of *Neisseria gonorrhoeae* PilB can use electrons from DsbD to reduce downstream methionine sulfoxide reductases. *J. Biol. Chem. 281*, 32668–32675.
8. Fabianek, R. A., Hennecke, H., and Thöny-Meyer, L. (1998) The active-site cysteines of the periplasmic thioredoxin-like protein in CcmG of *Escherichia coli* are important but not essential for cytochrome *c* maturation vivo. *J. Bacteriol. 180*, 1947–1950.
9. Fabianek, R. A., Huber-Wunderlich, M., Glockshuber, R., Künzler, P., Hennecke, H., and Thöny-Meyer, L. (1997) Characterization of the *Bradyrhizobium japonicum* CycY protein, a membrane-anchored periplasmic thioredoxin that may play a role as a reductant in the biogenesis of *c*-type cytochromes. *J. Biol. Chem. 272*, 4467–4473.
10. Loferer, H., Bott, M., and Hennecke, H. (1993) *Bradyrhizobium japonicum* TlpA, a novel membrane-anchored thioredoxin-like protein involved in the biogenesis of cytochrome aa_3 and development of symbiosis. *EMBO J. 12*, 3373–3383.
11. Erlendsson, L. S., Acheson, R. M., Hederstedt, L., and Le Brun, N. E. (2003) *Bacillus subtilis* ResA is a thiol-disulfide oxidoreductase involved in cytochrome *c* synthesis. *J. Biol. Chem. 278*, 17852–17858.
12. Ouyang, N., Gao, Y. G., Hu, H. Y., and Xia, Z. X. (2006) Crystal structures of *E. coli* CcmG and its mutants reveal key roles of the N-terminal β-sheet and the fingerprint region. *Proteins 65*, 1021–1031.
13. Edeling, M. A., Guddat, L. W., Fabianek, R. A., Thöny-Meyer, L., and Martin, J. L. (2002) Structure of CcmG/DsbE at 1.14 Å resolution: high-fidelity reducing activity in an indiscriminately oxidizing environment. *Structure 10*, 973–979.
14. Capitani, G., Rossmann, R., Sargent, D. F., Grütter, M. G., Richmond, T. J., and Hennecke, H. (2001) Structure of the soluble domain of a membrane-anchored thioredoxin-like protein from *Bradyrhizobium japonicum* reveals unusual properties. *J. Mol. Biol. 311*, 1037–1048.
15. Crow, A., Acheson, R. M., Le Brun, N. E., and Oubrie, A. (2004) Structural basis of redox-coupled protein substrate selection by the cytochrome *c* biosynthesis protein ResA. *J. Biol. Chem. 279*, 23654–23660.
16. Zhang, X., Hu, Y., Guo, X., Lescop, E., Li, Y., Xia, B., and Jin, C. (2006) The *Bacillus subtilis* YkuV is a thiol: disulfide oxidoreductase revealed by its redox structures and activity. *J. Biol. Chem. 281*, 8296–8304.
17. Bartels, C., Xia, T., Billeter, M., Güntert, P., and Wüthrich, K. (1995) The program XEASY for computer-supported NMR spectral analysis of biological macromolecules. *J. Biomol. NMR 6*, 1–10.
18. Keller, R. (2004) Optimizing the process of nuclear magnetic resonance spectrum analysis and computer aided resonance assignment, Ph.D. Thesis, Swiss Federal Institute of Technology, Zurich, Switzerland.
19. Wishart, D. S., Bigam, C. G., Yao, J., Abildgaard, F., Dyson, H. J., and Oldfield, E. (1995) ^{1}H,^{13}C and ^{15}N chemical shift referencing in biomolecular NMR. *J. Biomol. NMR 6*, 135–140.
20. Bai, Y., Milne, J. S., Mayne, L., and Englander, S. W. (1993) Primary structure effects on peptide group hydrogen exchange. *Proteins: Struct., Funct., Genet. 17*, 75–86.
21. Cordier, F., and Grzesiek, S. (2002) Temperature-dependence of protein hydrogen bond properties as studied by high-resolution NMR. *J. Mol. Biol. 317*, 39–52.
22. Cornilescu, G., Delaglio, F., and Bax, A. (1999) Protein backbone angle restraints from searching a database for chemical shift and sequence homology. *J. Biomol. NMR 13*, 289–302.
23. Siemion, I. Z., Wieland, T., and Pook, K. H. (1975) Influence of the distance of the proline carbonyl from the β and γ carbon on the ^{13}C chemical shifts. *Angew. Chem., Int. Ed. Engl. 14*, 702–703.
24. Guntert, P., Mumenthaler, C., and Wüthrich, K. (1997) Torsion angle dynamics for NMR structure calculation with the new program DYANA. *J. Mol. Biol. 273*, 283–298.
25. Guntert, P. (2004) Automated NMR structure calculation with CYANA. *Methods Mol. Biol. 278*, 353–378.
26. Koradi, R., Billeter, M., and Wüthrich, K. (1996) MOLMOL: a program for display and analysis of macromolecular structures. *J. Mol. Graphics 14*, 51–55.
27. Farrow, N. A., Muhandiram, R., Singer, A. U., Pascal, S. M., Kay, C. M., Gish, G., Shoelson, S. E., Pawson, T., FormanKay, J. D., and Kay, L. E. (1994) Backbone dynamics of a free and phosphopeptide-complexed Src homology 2 domain studied by ^{15}N NMR relaxation. *Biochemistry 33*, 5984–6003.
28. Johnson, B. A., and Blevins, R. A. (1994) NMRView: A computer program for the visualization and analysis of NMR data. *J. Biomol. NMR 4*, 603–614.
29. Farrow, N. A., Zhang, O., Szabo, A., Torchia, D. A., and Kay, L. E. (1995) Spectral density function mapping using ^{15}N relaxation data exclusively. *J. Biomol. NMR 6*, 153–162.
30. Ishima, R., Yamasaki, K., Saito, M., and Nagayama, K. (1995) Spectral densities of nitrogen nuclei in *Escherichia coli* ribonuclease HI obtained by ^{15}N NMR relaxation and molecular dynamics. *J. Biomol. NMR 2*, 217–220.
31. Ishima, R., and Nagayama, K. (1995) Protein backbone dynamics revealed by quasi spectral density function analysis of amide N-15 nuclei. *Biochemistry 34*, 3162–3171.
32. Lefevre, J. F., Dayie, K. T., Peng, J. W., and Wagner, G. (1996) Internal mobility in the partially folded DNA binding and dimerization domains of GAL4: NMR analysis of the N-H spectral density functions. *Biochemistry 35*, 2674–2686.
33. Hiyama, Y., Niu, C., Silverton, J. V., Bavoso, A., and Torchia, D. A. (1988) Determination of ^{15}N chemical shift tensor via ^{15}N-^{2}H dipolar coupling in Boc-glycylglycyl[^{15}N glycine]benzyl ester. *J. Am. Chem. Soc. 110*, 2378–2383.
34. Peng, J. W., and Wagner, G. (1995) Frequency spectrum of NH bond in eglin *c* from spectral density mapping at multiple fields. *Biochemistry 34*, 16733–16752.
35. Dosset, P., Hus, J.-C., Blackledge, M., and Marion, D. (2000) Efficient analysis of macromolecular rotational diffusion from heteronuclear relaxation data. *J. Biomol. NMR 16*, 23–28.
36. Lipari, G., and Szabo, A. (1982) Model-free approach to the interpretation on nuclear magnetic resonance relaxation in macromolecules. 1. Theory and range of validity. *J. Am. Chem. Soc. 104*, 4546–4559.

37. Lipari, G., and Szabo, A. (1982) Model-free approach to the interpretation on nuclear magnetic resonance relaxation in macromolecules. 2. Analysis of experimental results. *J. Am. Chem. Soc. 104*, 4560–4570.
38. Beaufils, C., Neiers, F., Coudevylle, N., Boschi-Muller, S., Averlant-Petit, M. C., Branlant, G., and Cung, M. T. (2006) ^{1}H, ^{13}C and ^{15}N resonance assignment of the N-terminal domain of PilB from *Neisseria meningitidis*. *J. Biomol. NMR 36*, 6.
39. Quinternet, M., Beaufils, C., Neiers, F., Tsan, P., Boschi-Muller, S., Averland-Petit, M.-C., Branlant, G., and Cung, M.-T. (2007) ^{1}H, ^{13}C and ^{15}N backbone resonance assignment of the oxidized form (Cys_{67}-Cys_{70}) of the N-terminal domain of PILB from *Neisseria meningitidis*. *Biomol. NMR Assign. 1*, 143–145.
40. Auguin, D., Barthe, P., Augé-Sénégas, M. T., Stern, M. H., Noguchi, M., and Roumestand, C. (2004) Solution structure and backbone dynamics of the pleckstrin homology domain of the human protein kinase B (PKB/Akt). Interaction with inositol phosphates. *J. Biomol. NMR 28*, 137–155.
41. Holm, L., and Sander, C. (1993) Protein structure comparison by alignment of distance matrices. *J. Mol. Biol. 233*, 123–138.
42. Gibrat, J. F., Madej, T., and Bryant, S. H. (1996) Surprising similarities in structure comparison. *Curr. Opin. Struct. Biol. 6*, 377–385.
43. Berman, H. M., Westbrook, J., Feng, Z., Gilliland, G., Bhat, T. N., Weissig, H., Shindyalov, I. N., and Bourne, P. E. (2000) The Protein Data Bank. *Nucleic Acids Res. 28*, 235–242.
44. Lancelin, J.-M., Guilhaudis, L., Krimm, I., Blackledge, M. J., Marion, D., and Jacquot, J.-P. (2000) NMR structures of thioredoxin *m* from the green alga *Chlamydomonas reinhardtii*. *Proteins 41*, 334–349.
45. Stone, M. J., Chandrasekhar, K., Holmgren, A., Wright, P. E., and Dyson, J. H. (1993) Comparison of backbone and tryptophan side-chain dynamics of reduced and oxidized Escherichia coli thioredoxin using ^{15}N NMR relaxation measurements. *Biochemistry 32*, 426–435.
46. Colbert, C. L., Wu, Q., Erbel, P. J. A., Gardner, K. H., and Deisenhofer, J. (2006) Mechanism of substrate specificity in *Bacillus subtilis* ResA, a thioredoxin-like protein involved in cytochrome *c* maturation. *Proc. Natl. Acad. Sci. U.S.A. 103*, 4110–4415.
47. Hass, M. A., Thuesen, M. H., Christensen, H. E., and Led, J. J. (2004) Characterization of μs-ms dynamics of proteins using a combined analysis of ^{15}N NMR relaxation and chemical shift: conformational exchange in plastocyanin induced by histidine protonations. *J. Am. Chem. Soc. 126*, 753–765.
48. Stirnimann, C. U., Grütter, M. G., Glockshuber, R., and Capitani, G. (2006) nDsbD: a redox interaction hub in the *Escherichia coli* periplasm. *Cell. Mol. Life Sci. 63*, 1642–1648.
49. Gouet, P., Courcelle, E., Stuart, D. I., and Metoz, F. (1999) ESPript: multiple sequence alignments in PostScript. *Bioinformatics 15*, 305–308.

BI800884W